Journal of Materiomics 8 (2022) 656–661

Contents lists available at ScienceDirect

Journal of Materiomics

journal homepage: www.journals.elsevier.com/journal-of-materiomics/

Research paper

Phase-modulated mechanical and thermoelectric properties of $Ag_2S_{1-x}Te_x$ ductile semiconductors

Liming Peng [a, b], Shiqi Yang [a, b], Tian-Ran Wei [c, **], Pengfei Qiu [a, d], Jiong Yang [e], Zhen Zhang [f], Xun Shi [a, b, *], Lidong Chen [a, b]

[a] State Key Laboratory of High Performance Ceramics and Superfine Microstructure, Shanghai Institute of Ceramics, Chinese Academy of Sciences, Shanghai, 200050, China
[b] Center of Materials Science and Optoelectronics Engineering, University of Chinese Academy of Sciences, Beijing, 100049, China
[c] State Key Laboratory of Metal Matrix Composites, School of Materials Science and Engineering, Shanghai Jiao Tong University, Shanghai, 200240, China
[d] School of Chemistry and Materials Science, Hangzhou Institute for Advanced Study, University of Chinese Academy of Sciences, Hangzhou, 310024, China
[e] Materials Genome Institute, Shanghai University, Shanghai, 200444, China
[f] Division of Solid-State Electronics, Department of Electrical Engineering, Uppsala University, 75237, Uppsala, Sweden

ARTICLE INFO

Article history:
Received 26 October 2021
Received in revised form
11 November 2021
Accepted 13 November 2021
Available online 17 November 2021

Keywords:
Thermoelectric materials
Ag_2S-Ag_2Te ductile semiconductors
Phase transition
Mechanical properties
Transport properties

ABSTRACT

By virtue of the excellent plasticity and tunable transport properties, Ag_2S-based materials demonstrate an intriguing prospect for flexible or hetero-shaped thermoelectric applications. Among them, $Ag_2S_{1-x}Te_x$ exhibits rich and interesting variations in crystal structure, mechanical and thermoelectric transport properties. However, Te alloying obviously introduces extremely large order-disorder distributions of cations and anions, leading to quite complicated crystal structures and thermoelectric properties. Detailed composition-structure-performance correlation of $Ag_2S_{1-x}Te_x$ still remains to be established. In this work, we designed and prepared a series of $Ag_2S_{1-x}Te_x$ ($x = 0$–0.3) materials with low Te content. We discovered that the monoclinic-to-cubic phase transition occurs around $x = 0.16$ at room temperature. Te alloying plays a similar role as heating in facilitating this monoclinic-to-cubic phase transition, which is analyzed based on the thermodynamic principles. Compared with the monoclinic counterparts, the cubic-structured phases are more ductile and softer in mechanical properties. In addition, the cubic phases show a degenerately semiconducting behavior with higher thermoelectric performance. A maximum $zT = 0.8$ at 600 K and bending strain larger than 20% at room temperature were obtained in $Ag_2S_{0.7}Te_{0.3}$. This work provides a useful guidance for designing Ag_2S-based alloys with enhanced plasticity and high thermoelectric performance.

1. Introduction

The rapid development of flexible and hetero-shaped electronic equipment, *e.g.*, wearable electronics and implantable devices, calls for compatible power generating techniques [1,2]. Deformable, non-flat thermoelectric (TE) technology that can directly convert the heat from curved hot surfaces into electricity has thus become a popular, promising solution [3–6]. For decades, the deformability or the complex shape of TE devices has been realized by designing special device structures [7] or using intrinsically flexible polymers [8]. Nonetheless, high-performance inorganic thermoelectric materials (*e.g.*, Bi_2Te_3 [9–11], PbTe [12–14]) are prevailingly brittle, which greatly limits the service of these materials in flexible and hetero-shaped circumstances.

Recently, exceptional room-temperature plasticity was found in a few inorganic semiconductors such as Ag_2S [15,16], InSe crystal [17–19], and ZnS crystal (in darkness) [20], offering a new option to integrate deformability together with semiconducting behavior and decent electrical properties. The plasticity grants the semiconductors with decent processibility, machinability and large deformability, somewhat like metals, which greatly expands the application realms [21]. Particularly, the Ag_2S-based solid solutions

** Corresponding author.
* Corresponding author. State Key Laboratory of High Performance Ceramics and Superfine Microstructure, Shanghai Institute of Ceramics, Chinese Academy of Sciences, Shanghai, 200050, China.
E-mail addresses: tianran_wei@sjtu.edu.cn (T.-R. Wei), xshi@mail.sic.ac.cn (X. Shi).
Peer review under responsibility of The Chinese Ceramic Society.

https://doi.org/10.1016/j.jmat.2021.11.007

or alloys show high zT and decent plasticity [22–26]. For the $Ag_2S_{1-x}Se_x$ system, the materials at room temperature adopt the same monoclinic structure ($P2_1/c$) with α-Ag_2S when $x \leq 0.6$, but turn to the orthorhombic Ag_2Se-like structure ($P2_12_12_1$) when $x \geq 0.7$ [24]. Generally, the substitution of Se for S enhances the thermoelectric performance but impairs the plasticity. Maximum $zT = 0.6$ at room temperature is obtained in brittle Ag_2Se while decent zT and plasticity can be realized in $Ag_2S_{0.4}Se_{0.6}$ compositions [24].

Compared to the Ag_2S–Ag_2Se materials, the Ag_2S–Ag_2Te system exhibits more complicated crystal/phase structures and transport properties [27–29]. A small amount of Te would induce the transition from the monoclinic to the cubic phase, which greatly enhances the thermoelectric performance while retaining the plasticity [28]. For higher Te content ($x = 0.5$–0.8), the materials show more complex structures (including some amorphous characters) and complicated transport properties [27,29]. Despite the knowledge on the Ag_2S–Ag_2Te alloys, the dependence of phase structures on Te alloying and temperature is not well understood. Furthermore, this phase-modulated variation in mechanical and transport properties remains to be explored.

In this work, we studied the phase and crystal structure, mechanical properties and thermoelectric performance of $Ag_2S_{1-x}Te_x$ polycrystalline materials. The content of Te is limited to $x \leq 0.3$ in this work to avoid the complicated mixed or glass-like structures, as well as potential stability concerns in materials with higher Te content. It is found that the compositional threshold of the monoclinic-to-cubic transition at ambient temperature is around $x = 0.16$. Both monoclinic and cubic $Ag_2S_{1-x}Te_x$ samples have good plasticity, and the cubic phase seems to be softer and more ductile. In addition, cubic $Ag_2S_{1-x}Te_x$ materials possess better electrical performance and lower lattice thermal conductivity. The zT reaches a maximum value of 0.8 at 600 K for $Ag_2S_{0.7}Te_{0.3}$.

2. Experiments

2.1. Sample preparation

A series of polycrystalline $Ag_2S_{1-x}Te_x$ ($x = 0$–0.3) ingots were prepared by melting and annealing techniques. High-purity elements Ag (shots, 99.999%, Alfa Aesar), S (pieces, 99.9999%, Alfa Aesar), and Te (shots, 99.999%, Alfa Aesar) were weighed out and then sealed in a quartz tube under vacuum. The quartz tubes were put in the furnace and heated to 1273 K in 20 h and held at this temperature for 12 h, then cooled down to 823 K in 30 h. After annealing at this temperature for 2 days, the furnace was cooled to 393 K and held at this temperature for 10 h. Then, the furnace was cooled to room temperature.

2.2. Characterization

The phase and crystal structures of $Ag_2S_{1-x}Te_x$ samples were examined by X-ray diffraction (XRD) analysis (D8 Advance, Bruker) and transmission electron microscopy (TEM, JEM-1400, JEOL) with selected area electron diffraction (SAED). Phase composition analysis was carried out by the scanning electron microscopy (SEM, Supra 55, ZEISS) equipped with energy dispersive spectrometer (EDS). Hall coefficient (R_H) was measured by using the Van der Pauw method (8400 Series, Lakeshore) with a magnetic field swept from −1 to 1 T. Hall carrier concentration (n_H) and Hall mobility (μ_H) were derived by the relations $n_H = 1/eR_H$ and $\mu_H = \sigma R_H$, respectively. Electrical conductivity (σ) and *Seebeck* coefficient (S) were measured using ZEM3 (Ulvac-Riko). Thermal conductivity was calculated from the formula $\kappa = \lambda C_p d$, where the thermal diffusivity λ was measured by using the laser flash method (LFA 457, Netzsch), the heat capacity C_p was derived from Dulong-Petit law, and the density d was measured by using the Archimedes method. The sound speed data were obtained on an ultrasonic measurement system (UMS-100, Ritec) with shear wave transducers of 5 MHz and longitudinal wave transducers of 10 MHz. Bending tests on the bulk specimens were conducted on a dynamic thermomechanical analyzer (DMA 850, TA instrument). The specimen size for bending test was about $2 \times 1 \times 10$ mm^3, with the loading rate of 1 N min^{-1}. Vickers-hardness test was carried out on a Vickers hardness tester (TUKON-2100B, Instron) under the load of 0.3 kgf. All specimens were cut directly from the as-prepared ingot.

2.3. Calculations

The first-principles calculations were carried out based on the projector augmented wave [30] method, as implemented in the Vienna *ab initio* [31–33] simulation package. The Perdew-Burke-Ernzerhof [34] formed generalized gradient approximation were adopted as the exchange-correlation functional. The cut-off energy of the plane-wave basis was 350 eV, and the convergence criterion for total energy was 10^{-4} eV. The modified Becke-Johnson potential [35] was utilized to get more accurate band gaps. We adopted a supercell with chemical formula $Ag_{16}S_8$ and $Ag_{16}S_7Te$ to mimic the pristine and Te-alloyed materials.

3. Results and discussion

3.1. Phase and crystal structures

The monoclinic and cubic crystal structures of Ag_2S are depicted Fig. 1a and 1b. Cations and anions fully occupy the fixed sites in monoclinic structure while the cations partially occupy the atomic sites in the cubic structure [36]. Fig. 1c shows the room-temperature XRD patterns for $Ag_2S_{1-x}Te_x$. The diffraction peaks for the samples with $x < 0.16$ are well indexed to the monoclinic structure with the space group of $P2_1/c$, isostructural with α-Ag_2S (Fig. 1a). When x exceeds 0.16, the materials transform into the cubic structure ($Im\bar{3}m$) that resembles the mid-temperature structure of Ag_2S (Fig. 1b). No impurity phases were detected by the XRD data for all $Ag_2S_{1-x}Te_x$ compounds. EDS analysis (Fig. 2a) also confirmed that Ag, S and Te are homogeneously distributed in the samples. Based on the above results, it can be concluded that the phase transition composition between the monoclinic and cubic structures in $Ag_2S_{1-x}Te_x$ alloys should be around $x = 0.16$ at 300 K.

According to the previous study [37], the S sublattice in the monoclinic structure can be viewed as a distorted *bcc* lattice with the β angle being 99°35′ rather than 90° (Fig. S1). The biggest difference between the monoclinic and cubic structures is the arrangement of silver atoms. In a unit cell of α-Ag_2S, four silver atoms occupy two different positions. However, it was reported that four silver atoms statistically occupy 42 positions in the unit cell of β-Ag_2S [37]. Such a random disorder of Ag atoms could be one of the key reasons that lead to the broad humps in the XRD patterns (Fig. 1c) and the amorphous ring in the selected area electron diffraction (SAED, Fig. 2c) of the cubic phase. Moreover, the SAED patterns of $Ag_2S_{0.94}Te_{0.06}$ (Fig. 2b) and $Ag_2S_{0.76}Te_{0.24}$ (Fig. 2c) well match the structure of monoclinic Ag_2S along $[00\bar{1}]$ and that of cubic Ag_2S along $[\bar{1}11]$ respectively, furtherly confirming the phase transition in $Ag_2S_{1-x}Te_x$ materials.

The synergetic effect on phase structures by Te content and temperature is studied by the differential scanning calorimetry (DSC) analysis (Fig. 1d). With Te content x increasing from 0 to 0.14, the monoclinic-to-cubic transition temperature decreases gradually from 450 K to 275 K. For $x = 0.16$, there are multiple continuous

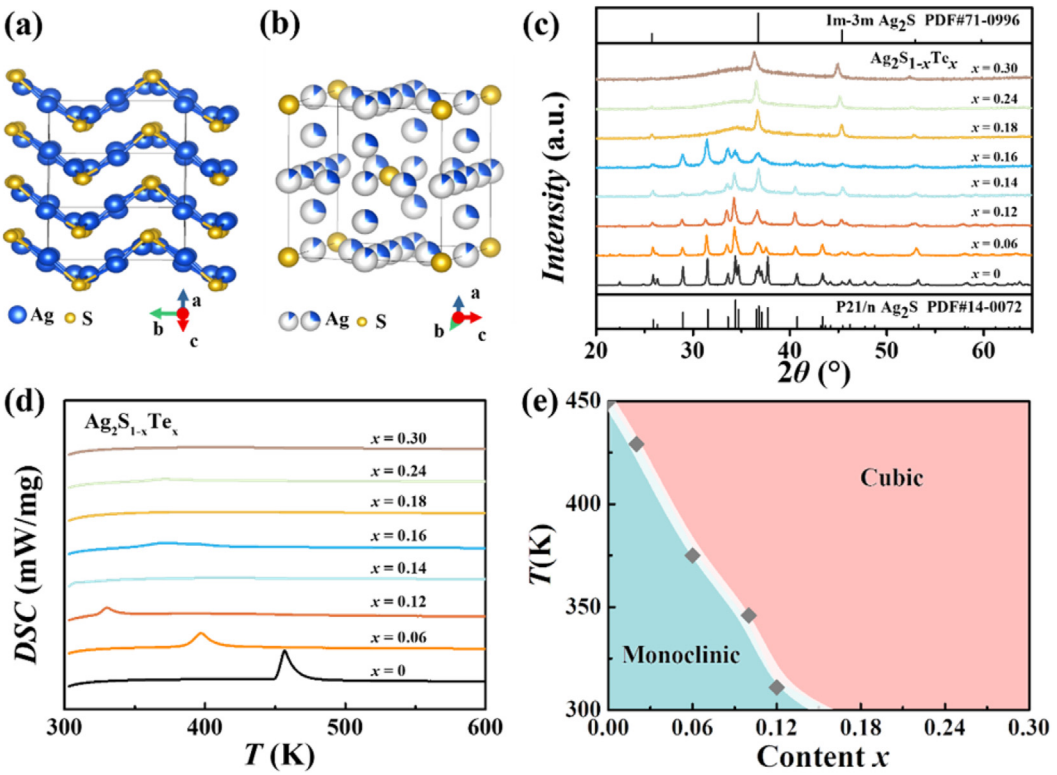

Fig. 1. Crystal structures of (a) monoclinic α-Ag_2S and (b) cubic β-Ag_2S. The crystallographic data were taken from refs. 15 and 36. The two different signs of Ag atoms in the cubic structure denote two types of Ag atoms with an occupancy of 26.7% and 14.6% at the 12d and 6b sites, respectively. (c) XRD patterns for bulk $Ag_2S_{1-x}Te_x$ ($x = 0–0.3$) samples. (d) DSC patterns for $Ag_2S_{1-x}Te_x$ materials. (e) Dependence of phase structure on temperature and Te content.

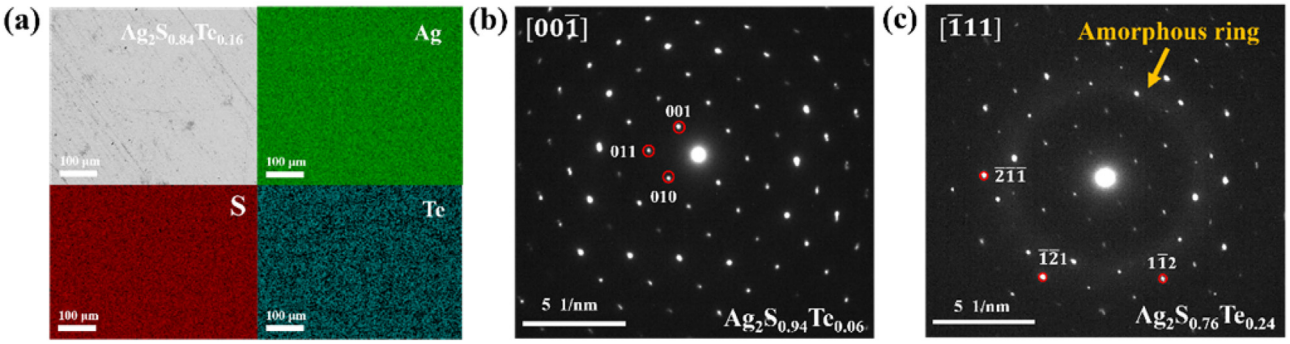

Fig. 2. (a) Backscattered electron (BSE) image and elemental energy dispersive spectroscopy (EDS) mappings of $Ag_2S_{0.84}Te_{0.16}$. Selected area electron diffraction (SAED) patterns of (b) $Ag_2S_{0.94}Te_{0.06}$ and (c) $Ag_2S_{0.76}Te_{0.24}$.

endothermic peaks, indicating the existence of mixed phases. When x reaches 0.18, no obvious peaks were observed above 300 K, indicating the pure cubic phase. Based on the experiment data, the "phase diagram" is thus depicted in Fig. 1e.

Te substitution plays a similar role as thermal annealing in facilitating the monoclinic-to-cubic transformation. This can be intuitively understood from the simple thermodynamic principles [38]. Due to the much more possible occupational options of Ag atoms, the cubic phase should exhibit a higher configuration entropy than the monoclinic one. According to the $G=H-TS$ relation, the Gibbs free energy decreases more sharply with temperature in the high-entropy phase; that is, the cubic phase is prone to be formed at higher temperatures (Fig. S2a). On the other hand, partial substitution of Te for S increases the configurations of the anion site to the same extent for cubic and monoclinic phases. Nonetheless, the total occupancy configurations of the system should be the multiplication of the occupancy configurations at the cation site and those at the anion site. Therefore, the increase in total entropy S or configurations by Te alloying is larger in the cubic phase that already has a larger number of cation states, leading to a lower Gibbs energy (Fig. S2b). It should be noted that the actual role of Te substitution in modifying the crystal structure should be more complicated than discussed above. For example, Ag–Te bond is weaker than the Ag–S bond, which may also promote the cation off site and disorder.

3.2. Mechanical properties

The room-temperature mechanical properties of $Ag_2S_{1-x}Te_x$ ($x = 0–0.3$) are shown in Fig. 3. Nearly all the samples exhibit large

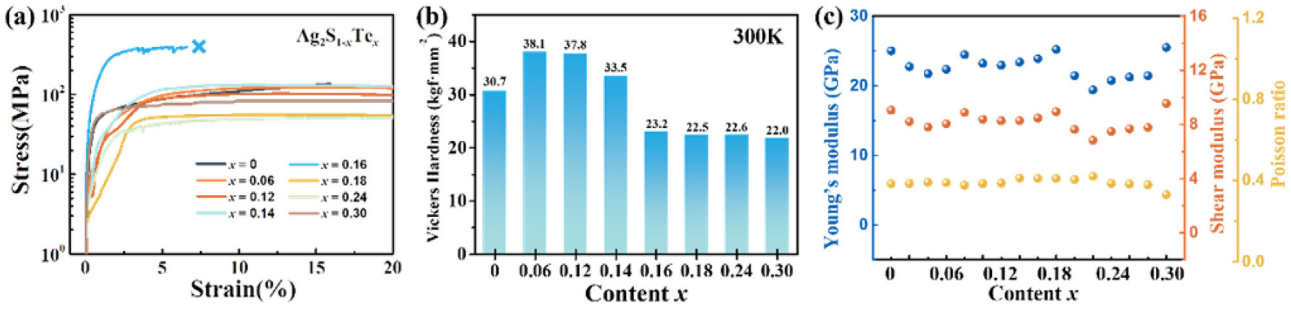

Fig. 3. (a) Stress–strain curves for bending test at 300 K. (b) Vickers Hardness under the load of 0.3 kgf and (c) Young's modulus, shear modulus and Poisson ratio derived from the measured sound speed; the calculation details are given in SI.

bending strains above 20% without fracture (Fig. 3a). The ultimate strain is lower (~7%) for the $x = 0.16$ sample, which may be related to the mixed phase structures hindering the dislocation slipping. A larger yield strength (around 400 MPa) is also observed for this sample. Generally, the yield strength is around 100 MPa for monoclinic samples, and 50 MPa for cubic phases. Consistently, the value of Vickers hardness decreases from 38.1 for $Ag_2S_{0.94}Te_{0.06}$ (monoclinic) to 22.5 for $Ag_2S_{0.76}Te_{0.24}$ (cubic) as shown in Fig. 3b. The better plastic deformability of the cubic phase can be understood from the lower generalized stacking fault energy (GSFE) as previously reported [28]. The elastic parameters (Young's modulus, shear modulus and Poisson's ratio) derived from measured sound speed, are roughly independent of Te content (Fig. 3c). The average sound velocity of $Ag_2S_{1-x}Te_x$ is as low as 1190 m/s, much smaller than most thermoelectric materials (such as 1691 m/s for $AgInTe_2$ [39], 2067 m/s for Cu_2Se [40], 3224 m/s for $CoSb_3$ [41]). This reflects a "soft" lattice of $Ag_2S_{1-x}Te_x$ and suggests a low lattice thermal conductivity.

3.3. Electrical transport properties

Fig. 4a–c shows the electrical transport properties of $Ag_2S_{1-x}Te_x$ materials. Te substitution changes the conduction behavior from the non-degenerate type ($x = 0$, 0.06) to the degenerate one ($x = 0.12$–0.3). Generally, the electrical conductivity (σ) increases and the *Seebeck* coefficient (S) decreases with Te content. Again, the mixed-phase sample with $x = 0.16$ shows an irregular conductivity. The abrupt change of σ and S vs. temperature in $x = 0$ and $x = 0.06$ samples should be caused by the monoclinic-to-cubic phase transition. The power factor (*PF*) at room temperature was greatly enhanced from 1.1×10^{-3} $\mu Wcm^{-1}K^{-2}$ for $x = 0$ to 4.8 $\mu Wcm^{-1}K^{-2}$ for $x = 0.3$. A maximum *PF* reaches 6.6 $\mu Wcm^{-1}K^{-2}$ at 600 K for $x = 0.24$ and 0.3.

The carrier concentration n_H and the mobility μ_H are shown in Fig. 4d. In the monoclinic realm, n_H increases sharply from the order of 10^{14} cm^{-3} for pristine Ag_2S to 10^{18} cm^{-3} for $x = 0.14$, which leads to the enhanced electrical conductivity, decreased *Seebeck* coefficient as well as the altered temperature dependence (Fig. 4a and **b**). The donor is believed to be the Ag interstitials or anion vacancies [42]. Since the Ag–Te bond is longer, weaker and less ionic than Ag–S bond, the defects are more prone to be formed in the Te-alloyed samples. In addition, 12.5% Te alloying at the S sites noticeably reduces the band gap (Fig. S3), which also contributes to the increased n_H. Interestingly, the mobility is roughly unchanged (~70 $cm^2V^{-1}s^{-1}$) by Te substitution in the monoclinic region, reflecting the compensating impacts from the sharpened band edge (reduced effective mass from 0.243 m_e for Ag_2S to 0.207m_e for $Ag_2S_{0.875}Te_{0.125}$) and the intensified alloy scattering of carriers.

Upon the phase transition, both n_H and μ_H largely increase from 1.4×10^{18} cm^{-3} and 81 $cm^2V^{-1}s^{-1}$ for $x = 0.14$ to 4×10^{19} cm^{-3} and 222 $cm^2V^{-1}s^{-1}$ for $x = 0.18$, respectively. In the cubic realm ($x > 0.16$), n_H moderately decreases while μ_H greatly increases with increasing Te content. Since it is difficult to accurately calculate the band structure of the complex cubic phase, here we tentatively explain this phenomenon through simple intuitions [43]. Te substitution for S should decrease the bond ionicity, which lowers the carrier effective mass. According to the single parabolic band (SPB) model [44], a smaller m^* substantially leads to the reduced carrier concentration and increased mobility for degenerate semiconductors.

3.4. Thermal transport and thermoelectric figure of merit

Fig. 5a shows the total thermal conductivities (κ) as a function of temperature for $Ag_2S_{1-x}Te_x$ samples. The pristine Ag_2S exhibits a low thermal conductivity of 0.47 $Wm^{-1}K^{-1}$ at RT. With Te alloying, κ increases from 0.45 $Wm^{-1}K^{-1}$ for $Ag_2S_{0.94}Te_{0.06}$ to 1.0 $Wm^{-1}K^{-1}$ for $Ag_2S_{0.82}Te_{0.18}$ at RT due to larger contribution of electronic thermal conduction. The discontinuous breaks in $x = 0$, 0.06 and 0.12 samples are ascribed to the phase transition. The lattice thermal conductivity κ_L was calculated via $\kappa_L = \kappa - L\sigma T$, where L is the Lorentz factor estimated based on the measured *Seebeck* coefficient. At room temperature, κ_L is 0.3–0.6 $Wm^{-1}K^{-1}$ for monoclinic phases ($0 \le x \le 0.14$) and decreases to 0.1–0.2 $Wm^{-1}K^{-1}$ for the cubic samples ($0.18 \le x \le 0.30$). The ultralow κ_L of the cubic phase is attributed to the disordered Ag ions loosely bonded to the anions, a demonstration of "electron crystal phonon glass (or liquid)" scenarios [45–50]. The zT as a function of temperature is shown in Fig. 5c. At room temperature, the highest zT is around 0.3 for $x = 0.3$. At 600 K, the zT of $Ag_2S_{0.7}Te_{0.3}$ sample is around 0.8, which is comparable to the reported results [28].

4. Conclusion

In conclusion, the correlation between composition, crystal/phase structure, thermoelectric and mechanical properties was established for $Ag_2S_{1-x}Te_x$ ($x = 0$–0.3) ductile semiconductors. Te substitution for S can effectively lower the monoclinic-to-cubic phase transition temperature. The compositional threshold for the phase transition at ambient temperature is around $x = 0.16$. Compared with the monoclinic phase, the cubic phase is more ductile and softer with better electrical performance and lower κ_L. The thermoelectric performance is also greatly improved by Te alloying. Maximum zT reaches 0.3 at 300 K and 0.8 at 600 K for the composition of $Ag_2S_{0.7}Te_{0.3}$. This study clarifies composition- and phase-dependent thermoelectric and mechanical properties of *S*-rich $Ag_2S_{1-x}Te_x$ system, which will advance the understanding and development of ductile semiconductors for flexible or hetero-

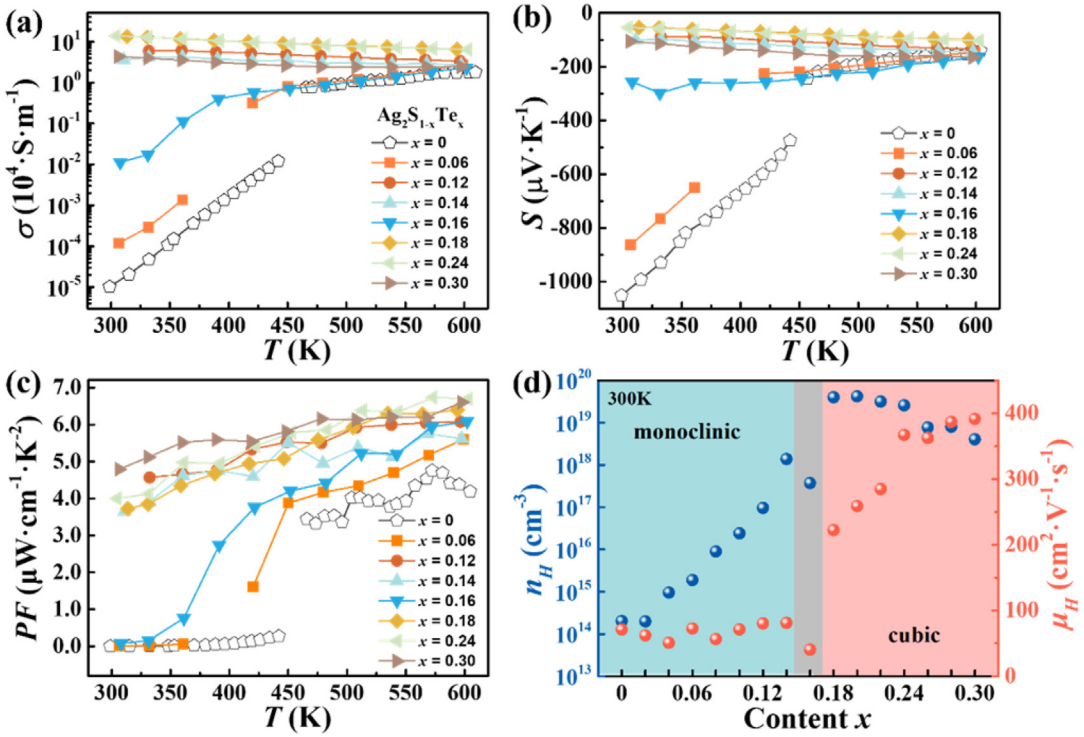

Fig. 4. Temperature dependence of (a) electrical conductivity (σ), (b) *Seebeck* coefficient (S), and (c) power factor (PF). (d) Te content dependence of carrier concentration (n_H) and mobility (μ_H) at 300 K for $Ag_2S_{1-x}Te_x$ samples.

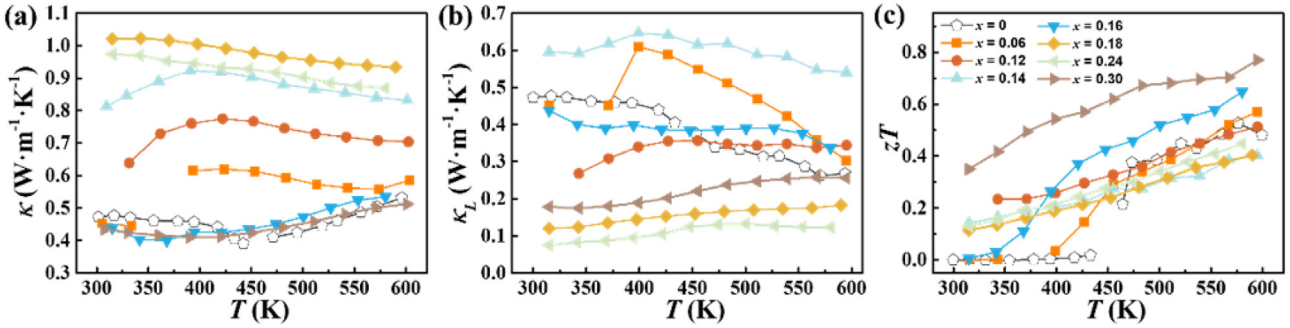

Fig. 5. Temperature dependence of (a) thermal conductivity (κ), (b) lattice thermal conductivity (κ_L), and (c) zT for $Ag_2S_{1-x}Te_x$.

shaped thermoelectric applications.

Declaration of competing interest

The authors declare that they have no known competing financial interests or personal relationships that could have appeared to influence the work reported in this paper.

Acknowledgements

This work is supported by the National Key Research and Development Program of China (2018YFB0703600), National Natural Science Foundation of China (91963208, 51625205, 51961135106, 51802333), the CAS-DOE Program of Chinese Academy of Sciences (121631KYSB20180060), the Shanghai Government (20JC1415100), and the Swedish Research Council (VR 2018–06030).

Appendix A. Supplementary data

Supplementary data to this article can be found online at https://doi.org/10.1016/j.jmat.2021.11.007.

References

[1] Nomura K, Ohta H, Takagi A, Kamiya T, Hirano M, Hosono H. Nature 2004;432:488–92.
[2] Rogers JA, Someya T, Huang Y. Science 2010;327:1603–7.
[3] Wang Y, Liu G, Sheng M, Yu C, Deng Y. J Mater Chem A 2019;7:1718–24.
[4] Wang Y, Yang L, Shi XL, Shi X, Chen LD, Dargusch MS, et al. Adv Mater 2019;31:1807916.
[5] Yang S, Qiu P, Chen L, Shi X. Small Science 2021;1:2100005.
[6] Ding Y, Qiu Y, Cai K, Yao Q, Chen S, Chen L, et al. Nat Commun 2019;10:841.
[7] Kim S, We J, Cho B. Energy Environ Sci 2014;7:1959–65.
[8] Zhang Q, Sun YM, Xu W, Zhu DB. Adv Mater 2014;26:6829–51.
[9] Pan Y, Aydemir U, Grovogui JA, Witting IT, Hanus R, Xu YB, et al. Adv Mater 2018;30:1802016.
[10] Xie W, Tang X, Yan Y, Zhang Q, Tritt TM. Appl Phys Lett 2009;94:102111.
[11] Hu L, Zhu T, Liu X, Zhao X. Adv Funct Mater 2014;24:5211–8.
[12] Pei YZ, Shi XY, LaLonde A, Wang H, Chen LD, Snyder GJ. Nature 2011;473:

66–9.
[13] Heremans J, Jovovic V, Toberer E, Saramat A, Kurosaki K, Charoenphakdee A, et al. Science 2008;321:554–7.
[14] Biswas K, He JQ, Blum ID, Wu CI, Hogan TP, Seidman DN, et al. Nature 2012;489:414–8.
[15] Shi X, Chen H, Hao F, Liu R, Wang T, Qiu P, et al. Nat Mater 2018;17:421–6.
[16] Li G, An Q, Morozov S, Duan B, Goddard W, Zhang Q, et al. npj Comput Mater 2018;4:44.
[17] Wei T, Jin M, Wang Y, Chen H, Gao Z, Zhao K, et al. Science 2020;369:542–5.
[18] Han X. Science 2020;369:509.
[19] Zhang B, Wu H, Peng K, Shen X, Gong X, Zheng S, et al. Chin Phys B 2021;30:078101.
[20] Oshima Y, Nakamura A, Matsunaga K. Science 2018;360:772–4.
[21] Chen H, Wei T, Zhao K, Qiu P, Chen L, He J, et al. Infomat 2021;3:22–35.
[22] Wang T, Zhao K, Qiu P, Song Q, Chen L, Shi X. ACS Appl Mater Interfaces 2019;11:12632–8.
[23] Liang J, Wang T, Qiu P, Yang S, Ming C, Chen H, et al. Energy Environ Sci 2019;12:2983–90.
[24] Liang J, Qiu P, Zhu Y, Huang H, Gao Z, Zhang Z, et al. Research 2020:6591981. 2020.
[25] Gao Z, Yang Q, Qiu P, Wei TR, Yang S, Xiao J, et al. Adv Energy Mater 2021;11:2100883.
[26] Liu J, Xing T, Gao Z, Liang J, Peng L, Xiao J, et al. Appl Phys Lett 2021;119:121905.
[27] He S, Li Y, Liu L, Jiang Y, Feng J, Zhu W, et al. Sci Adv 2020;6:eaaz8423.
[28] Yang S, Gao Z, Qiu P, Liang J, Wei T, Deng T, et al. Adv Mater 2021;33:2007681.
[29] Liang X, Chen C. Acta Mater 2021;218:117231.
[30] Blochl PE. Phys Rev B 1994;50:17953–79.
[31] Kresse G, Hafner J. Phys Rev B 1994;49:14251–69.
[32] Kresse G, Furthmuller J. Phys Rev B 1996;54:11169–86.
[33] Kresse G, Furthmuller J. Comput Mater Sci 1996;6:15–50.
[34] Perdew JP, Burke K, Ernzerhof M. Phys Rev Lett 1996;77:3865–8.
[35] Tran F, Blaha P. Phys Rev Lett 2009;102:226401.
[36] Cava R, Reidinger F, Wuensch B. J Solid State Chem 1980;31:69–80.
[37] Sadanaga R, Sueno S. Mineral Mag 1967;5:124–43.
[38] Borgnakke C, Sonntag R. Fundamentals of thermodynamics. John Wiley & Sons; 2020.
[39] Qiu P, Qin Y, Zhang Q, Li R, Yang J, Song Q, et al. Adv Sci 2018;5:1700727.
[40] Liu W, Yang L, Chen Z, Zou J. Adv Mater 2020;32:1905703.
[41] Caillat T, Borshchevsky A, Fleurial J. J Appl Phys 1996;80:4442–9.
[42] Zhou Y, Li X, Xi L, Yang J. J Materiomics 2021;7:19–24.
[43] Zeier WG, Zevalkink A, Gibbs ZM, Hautier G, Kanatzidis MG, Snyder GJ. Angew Chem Int Ed 2016;55:6826–41.
[44] May A, Snyder G. In: Thermoelectrics and its energy harvesting. Boca Raton: CRC Press; 2012.
[45] Liu H, Shi X, Xu F, Zhang L, Zhang W, Chen L, et al. Nat Mater 2012;11:422–5.
[46] Tan G, Hao S, Zhao J, Wolverton C, Kanatzidis MG. J Am Chem Soc 2017;139:6467–73.
[47] Zhao K, Qiu P, Shi X, Chen L. Adv Funct Mater 2019;30:1903867.
[48] Liu H, Yang J, Shi X, Danilkin SA, Yu D, Wang C, et al. J Materiomics 2016;2:187–95.
[49] Zhu TJ, Liu YT, Fu CG, Heremans JP, Snyder JG, Zhao XB. Adv Mater 2017;29:1605884.
[50] Deng T, Wei T, Huang H, Song Q, Zhao K, Qiu P, et al. npj Comput Mater 2020;6:81.

Liming Peng received his B.S. in materials science and engineering from Xiamen University. He is currently a Ph.D. candidate at Shanghai Institute of Ceramics, Chinese Academy of Sciences (SICCAS). His current research is mainly focused on Ag_2S-based ductile and flexible thermoelectric materials and devices.

Tian-Ran Wei is an associate professor at school of materials science and engineering, Shanghai Jiao Tong University (SJTU). He obtained his PhD from Tsinghua University in 2017. He was a visiting scholar at Northwestern University (USA) in 2015. He worked at SICCAS from 2017 to 2018 before joining SJTU. His current research focuses on novel ductile inorganic semiconductors and advanced thermoelectric materials.

Xun Shi is a professor at SICCAS. He received his B.S. (2000) in Tsinghua University and PhD (2005) in the University of Chinese Academy of Sciences. He worked at the University of Michigan (USA) as a postdoctor from 2007 to 2009. He then joined the R&D center in General Motors. Since 2010 he has been a professor at SICCAS. His current research focuses on advanced thermoelectric materials and devices, and flexible semiconductors.